Atmospheric Artefacts Correction With a Covariance Weighted Linear Model Over Mountainous Regions

Zhongbo Hu, *Student Member, IEEE,* Jordi J. Mallorquí, *Senior Member, IEEE,* Hongdong Fan

***Abstract*—Mitigating atmospheric phase delay is one of the largest challenges facing the differential synthetic aperture radar interferometry (DInSAR) community. Recently, many publications have studied correcting stratified tropospheric phase delay by assuming a linear model between them and topography. However, most of these studies have not considered the effect of turbulent atmospheric artefacts when adjusting the linear model to data. In this paper, we present an improved technique that minimizes the influence of turbulent atmosphere in the model adjustment. In the proposed algorithm, the model is adjusted to the phase differences of pixels instead of using the unwrapped phase of each pixel. In addition, the different phase differences are weighted as a function of its Atmospheric Phase Screen (APS) covariance estimated from an empirical variogram to reduce in the model adjustment the impact of pixel pairs with significant turbulent atmosphere. The good performance of the proposed method has been validated with both simulated and real Sentinel1-A SAR data in the mountainous area of Tenerife island, Spain.**

***Index Terms*—Synthetic aperture radar (SAR), Interferometric SAR (InSAR), APS, modelling.**

I. Introduction

DIFFERENTIAL synthetic aperture radar interferometry (DInSAR), also known as Persistent Scatters Interferometry (PSI), has proven to be a very powerful technique for measuring large-scale land deformations with centimeter to millimeter accuracy along the Line of Sight (LOS) direction. Their high accuracy is achieved in correspondence to the high phase quality of interferograms, assuming they are not influenced by other phase components. However, the differences in humidity, temperature and pressure between two acquisitions may cause additional fringes on differential interferograms that affect the estimation of the geophysical parameters. In order to estimate them more reliably, the effect of APS cannot be ignored.

This research work has been supported by the China Scholarship Council (Grant 201506420043) and by the Spanish Ministry of Economy, Industry and Competitiveness (MINECO), the State Research Agency (AEI), the European Funds for Regional Development (EFRD) under project TEC2017-85244-C2-1-P and the Natural Science Foundation of China (51574221). CommSensLab is Unidad de Excelencia Maria de Maeztu MDM-2016-0600 financed by the Agencia Estatal de Investigacin, Spain.

Zhongbo Hu and Jordi J. Mallorquí are with the CommSensLab, Department of Signal Theory and Communications (TSC), Universitat Politècnica de Catalunya (UPC), 08034 Barcelona, Spain (e-mail: zhongbo.hu@tsc.upc.edu; mallorqui@tsc.upc.edu).

Hongdong Fan is with China University of Mining and Technology, 221116 Xuzhou, China (e-mail: cumtfhd@gmail.com).

A previous study by Hanssen [1] showed that the atmospheric propagation delay in an interferogram can be categorized into vertical stratification and turbulence components mixing. In the former, APS correlates with topographic variations, while in the latter, APS presents a spatial correlation length that can typically be described by the slope of its power spectral density based on Kolmogorov's theory.

To remove the two categories of APS from interferograms, different methods have been developed for atmospheric compensation. They can be classified in three categories. The classical approaches in time series analysis take advantage of the properties of APS and deformation in the interferometric phase. Turbulent atmospheric phase artefacts are highly correlated in space, but they can be assumed to be uncorrelated in time. At the same time, the phase terms associated to deformation present a higher temporal correlation and, usually assumed, a lower spatial correlation. Thus, the phase terms coming from atmospheric artefacts can be estimated and partially removed from the interferometric phase by applying different spatial and temporal filters [2]–[5]. However, with no prior information about the atmospheric artefacts and/or the deformation signal characteristics, it is difficult to determine the proper shape/extension of the spatial filter and the optimal length of the temporal filter. In order to optimize the filtering approaches, some researchers have tried to obtain the statistical properties of the atmospheric artefacts from auxiliary data (such as numerical weather prediction (NWP) products) as a priori information [6]. It has been proved that this is an alternative method to improve atmospheric artefacts mitigation. Despite the fact that these filtering methods are simple and effective in some cases, the coupling between the non-linear deformation and the APS prevents the correct separation of the two. There is always the risk of filtering in excess the non-linear deformation or contaminating the time-series with atmospheric noise.

Other techniques use auxiliary data sets such as meteorological models or multispectral remote sensing data. The APS delay in each individual interferogram can be mitigated using the retrieved water vapors from MERIS data, MODIS data [7], [8], GPS [9]–[11] or forecast products from NWP [12], [13]. However, the main limitation of this technique is the lack of available water vapor data in areas covered by clouds. In cloudy areas, numerical models such as the Weather Research and Forecasting Model (WRF), the Fifth Generation Penn State/NCAR Mesoscale Model (MM5) and global atmospheric reanalysis data have been used for predicting atmospheric

conditions [14]–[18]. However, the accuracy of the predicted water vapor contents depends on the quality of the models and their input data [19].

Another class of techniques considers that APS is correlated with topography [20], which can happen in mountainous areas. Stratified APS contribution in interferograms can be modelled by analysing the phase-elevation relationship with a linear model [21]–[24]. To estimate the stratified APS more accurately, recent improvements have been made by analysing phase-elevation relationship with a multiple-regression model [25]. In addition, a power law model has also been applied to remove tropospheric APS, which accounts for the spatial variation of the tropospheric properties [26]. The main limitation of these model related methods is that other phase terms (e.g. turbulent atmospheric artefacts, deformation related phase, decorrelation noise, ...) can influence the estimate of the coefficient that relates phase with elevation. In practice, Persistent Scatters (PSs) are usually selected to calculate the coefficient in order to reduce the impact of decorrelation noise. Although such attempt can be more effective to some extent [27], the influence of turbulent atmospheric artefacts can not be neglected. If the real situation fails to meet the basic assumption that the observed phase is stratified APS only, or in other words if the stratified and turbulent APS are mixed, current phase-elevation based methods may obtain an incorrect coefficient estimation.

From the aforementioned research, filtering approaches always aim at turbulent APS estimation, while modelling methods can estimate and mitigate the topography-related APS to some extent. Ancillary data, like weather forecast models, can partially provide both turbulent and stratified signals. Each type of method has its advantages and drawbacks. Stratified APS can influence the performance of the filtering-based methods. On the contrary, estimating stratified components using conventional linear models is not accurate in situations where the turbulent component exists.

This paper focuses on a new stratified APS correction technique that can be applied to mountainous areas in which the topography-related and turbulent APS are mixed together. As the turbulent component is correlated in space while the stratified one is correlated with topography, the proposed method is based on utilizing the phase differences among nearby pixels, which are within the correlation distance of turbulent APS, to estimate the coefficient value of a linear model. The biggest improvement of this technique is that the influence of turbulent components are minimized when modelling the stratified APS.

This paper is structured as follows. Section II describes the details of the compensation algorithm. In Section III, a simulated scenario is used to evaluate the proposed method with synthetic data. An analysis of the performance of the improved model with real data is shown in section IV. Finally, section V is dedicated to summarizing the main improvements and limitations of the APS compensation strategy.

II. Improved linear model: concept and algorithm

A. Motivation of APS Removing

In an interferogram, the differential phase of each pixel, ϕ, can be decomposed into five phase components [1], [2], [5], [28].

$$\phi = \phi_{\Delta topo} + \phi_{def} + \phi_{\Delta atm} + \phi_{orbit} + \phi_{noise} \quad (1)$$

Where $\phi_{\Delta topo}$ is the residual topographic phase caused by inaccuracies of the DEM used to generate the differential interferograms; ϕ_{def} is the phase contribution due to target displacement along the LOS direction; $\phi_{\Delta atm}$ relates to the differential atmospheric delays phase, which can be further decomposed into stratified delay ϕ_{atm_stra} and turbulent component ϕ_{atm_turb}; ϕ_{orbit} is the phase due to inaccuracies in the orbits; and ϕ_{noise} includes all phase terms caused by the different decorrelation factors.

All PSI algorithms have been struggling to get the reliable components of $\phi_{\Delta topo}$ and ϕ_{def}. In (1), ϕ_{orbit} phase component can be compensated using control points, and ϕ_{noise} phase is random, which is difficult to model for most of the decorrelation factors. As we work with persistent scatterers, which means that ϕ_{noise} shows a low variance, we ignore the ϕ_{noise} phase component. Consequently, $\phi_{\Delta atm}$ phase component is the main factor that limits the estimation of geophysical parameters.

B. Atmospheric Artefacts

Interferometric SAR (InSAR) observations are usually plagued by propagation delays. As the atmosphere properties (temperature, pressure, and relative humidity) between the radar platform and the ground targets vary spatially and temporally, the phase delays vary from one situation to another. At microwave bands it is well known that propagation delays have two major sources: tropospheric terms and ionosphere effects [1], [29]. For C-band and X-band data, the tropospheric component is the one with the most significant contribution to APS. On the contrary, with L-band SAR data over scenes located at high latitudes the ionosphere delays have also to be taken into consideration [30]. In this study focused in C-band data, the phase delay caused by the ionosphere is ignored.

The tropospheric delay can be elaborated that the velocity of electromagnetic waves is not constant through a heterogeneous medium as the speed of propagation changes with the refractivity index N of the medium. As the troposphere is mainly characterised by wet and hydrostatic components, the refractivity index N includes both. N_{dry} depends on partial pressure of dry air P, and N_{wet} is described by water vapour partial pressure e. Both refractivity components depend on temperature T. The refractivity can be mathematically characterised as: [31]

$$\begin{aligned} N(T,P,e) &= k_1\frac{P}{T} + k_2\frac{e}{T} + k_3\frac{e}{T^2} \\ &= N_{dry} + N_{wet} \end{aligned} \quad (2)$$

Where $k_1 = 0.776KPa^{-1}$, $k_2 = 0.716KPa^{-1}$, and $k_3 = 3.75e3K^2Pa^{-1}$.

The two-way propagation phase delay term, ϕ_{atm}, corresponds to the integration of the total refractivity $N(T,P,e)$ along the LOS:

$$\phi_{atm} = \frac{-4\pi}{\lambda} 10^{-6} \int_{\vec{x}_{target}}^{\vec{x}_{sat}} (N_{dry} + N_{wet}) dx \tag{3}$$

Where λ is the radar wavelength, $\vec{x}_{target}$ the location of the target and $\vec{x}_{sat}$ the zero-doppler location of the satellite for the target. In practice, it is not necessary to integrate along the whole path but only the extension of the troposphere [1]. For InSAR, the differential atmospheric delays $\phi_{\Delta atm}$ component is the difference between the two acquisitions.

In mountainous regions, topography dependent fluctuations of atmospheric parameters such as temperature, pressure and relative humidity lead to a variation of the atmospheric properties. Other publications show that stratified atmospheric delay $\phi_{\Delta atm\_stra}$ can be modelled as a linear relation with height [20]–[24], [27].

C. A Weighted Linear Model to Estimate Stratified APS

As mentioned in the previous section, in mountainous areas stratified APS linearly correlates with topography, which can be modelled as follows [20]–[24], [27]:

$$\phi_{model} = Kh + \phi_0 \tag{4}$$

Where K is the key coefficient to be estimated; h is the elevation, which can be derived from an auxiliary DEM (e.g. SRTM); and ϕ_0 is a phase offset.

As the phase quality of any interferogram is not homogeneous due to the different decorrelation sources, K has to be estimated from a set of high quality pixels, this is PSs. As resolution is not a constrain, the quality of the interferograms can be improved with multi-looking and the PSs selected imposing a simple coherence threshold. Since the coefficient K is assumed to be constant in a specific interferogram, it is possible to obtain a good estimation of K by adjusting the linear model (4) to the observation phase ϕ_{obs}. The coefficient K can be estimated by minimizing a Model Adjustement Function (MAF) [28] defined as follows:

$$\Gamma = \frac{1}{N} \sum_{i=1}^{N} \left| e^{-j\phi^i_{obs}} - e^{-j\phi^i_{model}} \right|^2 \tag{5}$$

Where N is the number of selected PSs. The mean advantage of working in the complex space is that it can be done with wrapped interferograms, so no phase-unwrapping is necessary and a potential source of errors is avoided.

Other papers dealing with the estimation of coefficient K have been published in the last years [22], [24]. In [22], a preliminary deformation is estimated and removed prior the calculation of K to avoid the "noise" contribution of deformation. Alternatively, in [24], improvements have been made by analysing the observed phase with a multiple spatial scales approach. Using these methodologies, topography related APS can be estimated correctly with the assumption that there is no turbulent APS in the phase ϕ_{obs}. Unfortunately, if the interferogram contains turbulent artefacts the estimation of K will be jeopardized.

In order to make more robust the model adjustment in presence of turbulent APS, in this paper it is proposed to use phase differences among the selected PSs instead of the absolute values. This improved method has been called Linear Model Resisting Turbulent Atmosphere Delay (LMRTA). Under LMRTA approach, it is possible to reduce the impact of turbulent APS significantly.

The implementation of the LMRTA is presented below. Considering the situation with turbulent APS, the observation phase ϕ_{obs} consists of ϕ_{atm_stra} and ϕ_{atm_turb} components.

$$\phi_{obs} = \phi_{atm\_stra} + \phi_{atm\_turb} \tag{6}$$

As ϕ_{atm_stra} component correlates with topography, namely it satisfies (3), but ϕ_{atm_turb} component not, adjusting directly the model ϕ_{model} with the observation phase ϕ_{obs} may lead to an incorrect coefficient K. Taking advantage of the spatial correlation of ϕ_{atm_turb}, the differential phases among neighbouring pixels can be used instead. A new observation phase between two pixels i and j, $\Delta\phi^{i,j}_{obs}$, can be defined to reduce the impact of turbulent APS in the model adjustment. The new phase is defined as,

$$\begin{aligned} \Delta\phi^{i,j}_{obs} &= \Delta\phi^{i,j}_{atm\_stra} + \Delta\phi^{i,j}_{atm\_turb} \\ &= \phi^i_{atm\_stra} - \phi^j_{atm\_stra} + \phi^i_{atm\_turb} - \phi^j_{atm\_turb} \end{aligned} \tag{7}$$

Correspondingly, LMRTA model can be defined now as

$$\begin{aligned} \Delta\phi^{i,j}_{model} &= Kh^i - Kh^j + \phi^i_0 - \phi^j_0 \\ &= K(h^i - h^j) \end{aligned} \tag{8}$$

ϕ_0 is a constant value for all pixels of the interferogram. Under the practical point of view, the selected pixels can be related thanks to a Delauney triangulation, where the pixel locations constitute the nodes and the relations among them the arcs. These arcs define the phase differences to be used during the model adjustment step. Different limitations can be set to improve the performance of K estimation, for instance the maximum arc length or the minimum number of arcs reaching any pixel of the triangulation.

Many studies indicate that the turbulent atmospheric artefacts correlate spatially [1]. The level of correlation decreases as the pixels' distance increases. Therefore, when estimating the coefficient of stratified APS, the influence of $\Delta\phi^{i,j}_{atm\_turb}$ component can be partially weakened by weighting in the MAF the different pixel pairs. The farther the pixels the lower its weight in MAF. To be more specific, for two close pixels i and j located at short distance the turbulent term for each one is very similar, so $\Delta\phi^{i,j}_{atm\_turb}$ should be close to zero. On the contrary, for other pixels with a large separation, the turbulent APS may be totally uncorrelated and the impact of $\Delta\phi^{i,j}_{atm\_turb}$ in MAF is considerable. Based on this concept, an appropriate covariance matrix involving the correlation length would be beneficial for weighting the different pixels' pairs.

D. Spatial Covariance Matrix

Previous studies show that a stochastic model can be used to properly characterise turbulent atmosphere phase delay [32]. Turbulent atmosphere artefacts are characterised by its

high spatial correlation. In spatial statistics the theoretical variogram is a function that describes the degree of spatial dependence of a spatial random field. So it is actually the variogram of atmospheric artefacts that can characterise the correlation of turbulent APS.

In geostatistics the empirical variogram is an estimate of the theoretical variogram and measures the spatial variability of an isotropic and stationary area. The empirical variogram $\hat{\gamma}(h)$ is defined as [33]:

$$\hat{\gamma}(l) = \frac{1}{2|N_l|} \sum_{(i,j)\in N_l} |z_i - z_j|^2 \tag{9}$$

Where N_l is the set of pairs of pixel i, j within distance l, $|N_l|$ is the total number of pairs within distance l and z would be in this case the turbulent atmospheric phase value. In practice, the turbulent phase is mixed with other components that are expected to be less correlated in space. Hence, the variogram of the turbulent atmospheric artefacts can be empirically estimated from the interferograms.

The turbulent atmospheric covariance matrix Σ of one interferogram can be derived from the empirical variogram.

$$\Sigma = \begin{pmatrix} \sigma^2_{11,11} & \sigma^2_{11,12} & \cdots & \sigma^2_{11,1m} & \sigma^2_{11,21} & \sigma^2_{11,22} & \cdots & \sigma^2_{11,nm} \\ \sigma^2_{21,11} & \sigma^2_{21,12} & \cdots & \sigma^2_{21,1m} & \sigma^2_{21,21} & \sigma^2_{21,22} & \cdots & \sigma^2_{21,nm} \\ \vdots & \vdots & \ddots & \vdots & \vdots & \vdots & \ddots & \vdots \\ \sigma^2_{n1,11} & \sigma^2_{n1,12} & \cdots & \sigma^2_{n1,1m} & \sigma^2_{n1,21} & \sigma^2_{n1,22} & \cdots & \sigma^2_{n1,nm} \\ \sigma^2_{12,11} & \sigma^2_{12,12} & \cdots & \sigma^2_{12,1m} & \sigma^2_{12,21} & \sigma^2_{12,22} & \cdots & \sigma^2_{12,nm} \\ \sigma^2_{22,11} & \sigma^2_{22,12} & \cdots & \sigma^2_{22,1m} & \sigma^2_{22,21} & \sigma^2_{22,22} & \cdots & \sigma^2_{22,nm} \\ \vdots & \vdots & \ddots & \vdots & \vdots & \vdots & \ddots & \vdots \\ \sigma^2_{nm,11} & \sigma^2_{nm,12} & \cdots & \sigma^2_{nm,1m} & \sigma^2_{nm,21} & \sigma^2_{nm,22} & \cdots & \sigma^2_{nm,nm} \end{pmatrix} \tag{10}$$

where n, m are the maximum pixel indices in azimuth and range directions respectively. Each element $\sigma^2_{hi,jk}$ in the covariance matrix can be derived as follows:

$$\sigma^2_{hi,jk} = \sigma^2(0) - \hat{\gamma}_{hi,jk}(l) \tag{11}$$

Where $\sigma^2(0)$ is the covariance at distance $l = 0$. In practice, $\sigma^2(0)$ is the limit of the variogram tending to infinity lag distances, and $h, j \in \{1, 2, \ldots, n\}, i, k \in \{1, 2, \ldots, m\}$. $\hat{\gamma}_{hi,jk}(l)$ is calculated from (9).

Once the covariance matrix of turbulent APS has been estimated, it can be used to weight the different arcs of the triangulation when adjusting the LMRTA model.

In real situations, three aspects limit the accurate variogram-based estimation of the turbulent APS covariance matrix: the density and quality of PSs, the real shape of the variogram, and the last but not the least, the different phase components present in the interferograms that can disguise the turbulent APS [34].

III. Validation With Simulated Data

The LMRTA method proposed in this paper is being validated firstly with simulated data in order to perform tests under perfectly controlled conditions. In comparison with real data cases, the true values of the different parameters involved are known, which can be compared with the estimated ones. In the simulated test, firstly, both topography related APS and turbulent APS are simulated. Secondly, the method aforementioned has been implemented to separate stratified APS from turbulent APS. Finally, an accuracy study has been done to evaluate the results of the new method compared with those of the conventional one.

A. Simulation of the Different Phase Components

The following synthetic scenario is simulated based on the parameters presented in Table I. Details on how to simulate the different atmospheric components are discussed.

TABLE I
PARAMETERS OVER A SYNTHETIC SCENARIO

Parameters	Value
Size of Images (pixels)	256 x 256
Number of Images	51
Number of Interferograms	135
Minimum temporal baseline (days)	11
Size of pixels (m)	30
Number of pixels	726
Number of links	2132
Maximum coefficient	0.2
Minimum coefficient	0.16
Standard deviation of coefficient	0.01
Maximum topography (m)	2000
Minimum topography (m)	1600

On the one hand, in terms of the turbulent atmospheric artefacts from the previous sections it is clear that the spatial variance is the key point. A large number of methods have been exploited to simulate Gaussian random fields [35], [36]. In these approaches, the spatial correlation matrix has to be firstly defined, and then the Cholesky decomposition can be applied to a random process [32] or the circular embedding method [35] can be used to Gaussian stochastic simulations. As mentioned in the previous sections, Kolmogorov's theory can generally describe the turbulent atmospheric artefacts and the spatial correlation follows approximatively an exponential law. In addition, a wide range of correlation models can describe the Kolmogorov's turbulence, which include Matérn-family models, Bessel family models, Guassian, exponential and spherical models. Different models are compared in [37]. In the following, the covariance of turbulent atmospheric artefacts has been simulated through a spherical model.

$$\gamma(l) = \begin{cases} \sigma^2(0)[\frac{3l}{2a} - \frac{1}{2}(\frac{l}{a})^3], & l \le a \\ \sigma^2(0), & l > a \end{cases} \tag{12}$$

Where $\sigma^2(0)$ means the variogram value for distances far away from the correlation distance, l is the distance and a indicates the correlation window. Examples of simulated turbulent atmospheric artefacts are shown in Fig. 1a and 1c.

On the other hand, the topography related atmospheric artefacts are modelled using a simple linear model. For simplicity, a topography based on a paraboloid and a semi-empirical coefficient K are chosen in the simulated scene. Examples of simulated topography related atmospheric artefacts are shown in Fig. 1b and 1d. We refer them as pair I1 and I2.

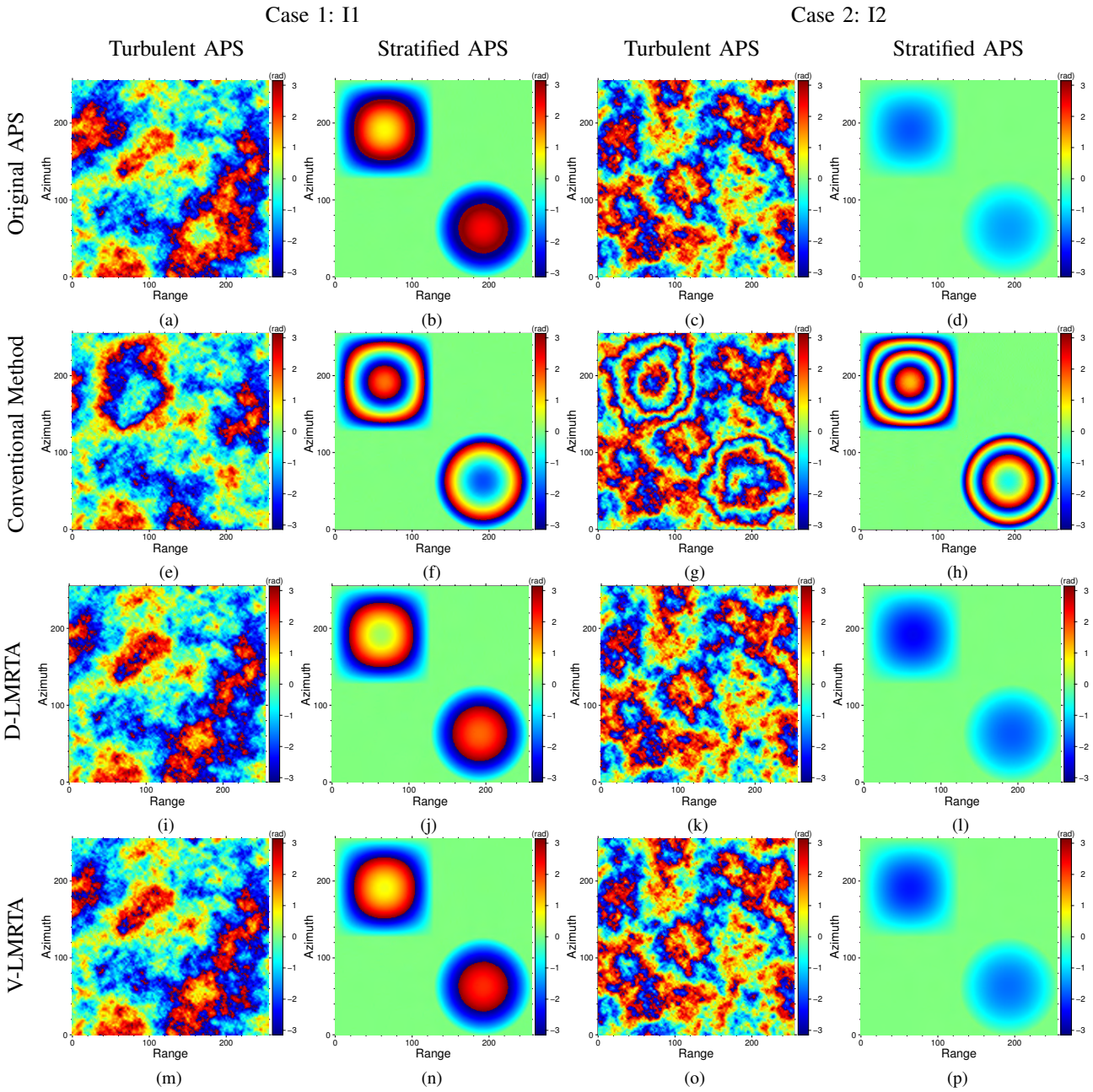

Fig. 1. Two examples of true and estimated turbulent APS (first and third column) and topography related APS (second and fourth column). The first two columns are for I1 and last two columns are for I2. The first row subfigures are for original APS, second row for conventional method, third row for distance weighted D-LMRTA and last row for variogram weighted V-LMRTA.

B. Stratified Atmospheric Artefacts Estimation

The first step of the algorithm is to select pixels with good phase quality, this is the PSs. The classical PSs coherence-based selection over the multi-looked interferograms can be used. The number of PSs selected will depend on the coherence threshold and the particularities of the interferogram. Once selected, they are connected using a Delaunay triangulation, as explained in Section II-C. In the simulation, 726 pixels have been randomly selected. The selected pixels and triangulation are shown in Fig. 2.

As mentioned previously, experimental variograms of APS are important to provide the parameters that characterise the spatial properties of turbulent atmospheric artefacts. In the simulated case, equation (9) has been used to do the variogram analysis. In the network of selected pixels, the minimal and maximal distances are 30 m and 10380 m respectively. Distance bins have been set to 30 m wide, the same resolution of the interferogram, in the variogram computation. The variograms calculated from the simulated turbulent APS I1 and I2 are shown in Fig. 3. Variogram values for arcs larger than 8 km are not represented as the number of pixels was too few for providing a reliable estimation. As it can be seen, that the variogram values for distances over 3 km show an oscillation behavior around a specific value, $\sigma^2(0)$. In other words, both plots in Fig. 3 show that the correlation distance of the atmospheric artefacts is about 3 km. The values

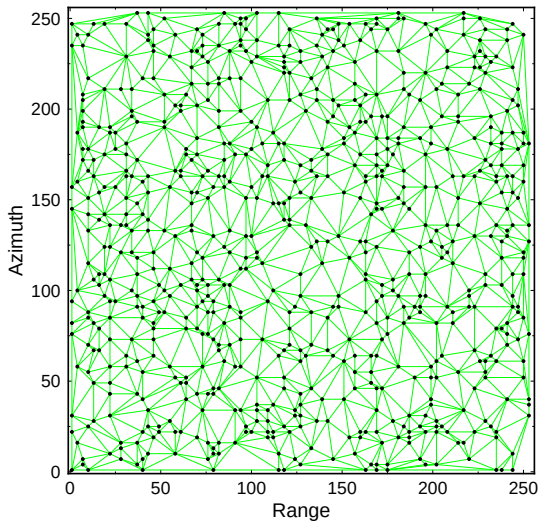

Fig. 2. Delaunay triangulation for selected PSs in the simulator.

of $\sigma^2(0)$ for I1 and I2 are 3.4 mm^2 and 5.8 mm^2 respectively, which is the average of variogram values for distance over 3 km for each case. Finally, the covariance matrix Σ for each interferogram can be filled using equation (11).

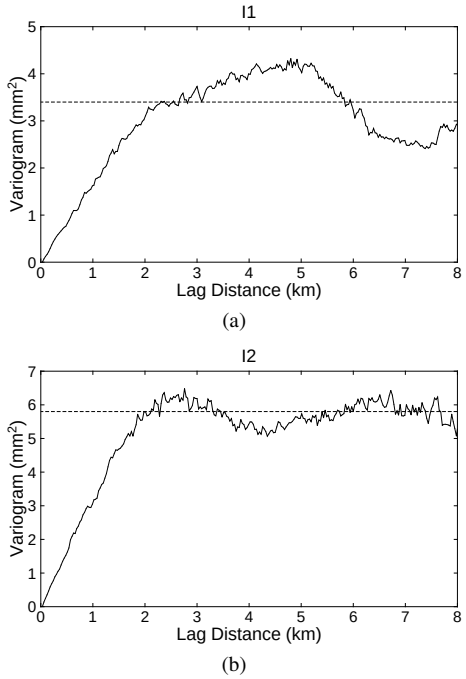

Fig. 3. Experimental variograms (dots) for turbulent APS I1 and I2. Dashed lines indicate $\sigma^2(0)$ for both cases.

In the following, both conventional method and the LMRTA method are applied to the synthetic data to separate the stratified and the turbulent APSs. The optimal coefficient K_{opt} can be estimated by a brute-force method testing all reasonable values of K_{opt} in $[-1, 1]$ with a step of 0.0001 in function $\Gamma(K)$.

$$K_{opt} = arg \min_{K\in[-1,1]} \Gamma(K) \tag{13}$$

The LMRTA algorithm uses the phase differences among connected pixels as a new observation phase to mitigate the impact of turbulent APS. In order to further reduce its impact, each arc can be weighted in such a way that the contribution of short distance pairs (less affected by turbulent APS) is increased in front of longer ones (more affected by turbulent APS). Based on this idea, the LMRTA algorithm can be improved by considering a weight matrix. Consequently, the MAF can be rewritten as follows.

$$\Gamma(K) = \frac{1}{\sum_{l=1}^{L} w_{i,j}} \sum_{i=1}^{L} \left| w_{i,j}(e^{-j\Delta\phi_{obs}^{i,j}} - e^{-j\Delta\phi_{model}^{i,j}}) \right|^2 \}) \tag{14}$$

Where L is the number of total arcs established among pixels and $w_{i,j}$ is its weight. $\Delta\phi_{obs}^{i,j}$ and $\Delta\phi_{model}^{i,j}$ are detailed in equations (7) and (8) respectively. The best weighting strategy would be to use the covariance matrix Σ derived from the empirical variogram, as presented in Section II-D. However, with real data covariance matrix can be costly to build in large scenes and prone to errors depending on the interferograms' quality. Alternatively, links' distances can be used as a practical alternative for determining the weight for each link. Namely, pairs with short distances are assigned higher weights than pairs with longer distances.

C. Evaluation of Results and Sensitivity Analysis

Fig. 1(a) – Fig. 1(d) show the original APS for two different cases with both turbulent and stratified atmosphere. Fig. 1(e) – 1(h) show the estimated turbulent APS and topography related APS obtained using the conventional method. Visually comparing with the true APS, the errors in the estimation of the stratified APS, which are translated to the estimation of the turbulent APS, are clearly visible. The benefits of the two versions of LMRTA, the Distance Weighted LMRTA (D-LMRTA) and the Variogram Weighted LMRTA (V-LMRTA), are evident from a visual comparison of the results with the original APS. Fig. 1(i) – 1(l) show the results for D-LMRTA while Fig. 1(m) – Fig. 1(p) for V-LMRTA.

Table II shows a comparison of the true and estimated values of K for the different methods. As it can be seen, the estimated coefficients for D-LMRTA and V-LMRTA are closer to the true values than the conventional method demonstrating the robustness of the proposed strategy when turbulent APS is presented. The performance of D-LMRTA and V-LMRTA is very similar, thus the distance-based weighting is an efficient alternative to avoid the the calculation of the covariance matrix of turbulent APS from the empirical variogram.

TABLE II
TRUE AND ESTIMATED COEFFICIENTS. K IS THE TRUE VALUE, WHILE K_1, K_2, K_3 ARE THE ESTIMATED RESULTS USING CONVENTIONAL METHOD, D-LMRTA AND V-LMRTA.

Interferograms	True K	Conventional K_1	D-LMRTA K_2	V-LMRTA K_3
I1	0.0100	0.0273	0.0151	0.0140
I2	0.0046	0.0442	0.0061	0.0056

It is also interesting to study the sensitivity of the minimization step to demonstrate the robustness of LMRTA approach. Fig. 4(a) and Fig. 4(b) show the behaviour of MAF,

$\Gamma(K)$, for the conventional and D-LMRTA methods when interferograms have stratified atmosphere only. The absence of the turbulent component allows both methods to find the exact value but conventional method is more sensitive. The quadratic behaviour of the function near the minimum is narrower than with D-LMRTA. The differences arise when turbulent APS and a linear deformation pattern are added to the interferograms. Fig. 5 shows the deformation pattern added to the interferograms, which covers the center of the scene. The results shown in Fig. 4(c) and Fig. 4(d) validate the robustness of D-LMRTA. D-LMRTA is able to retrieve a good approximation of the correct K while the conventional method fails. Looking at the plots, also the conventional method presents many local minima. This will make the minimization results very sensitive to any additional source of noise presenting in the interferometric phase. The linear deformation phase contribution definitely contaminates the estimation of K with the conventional method. However, the same advantages of D-LMRTA (or V-LMRTA) in front of turbulent APS, thanks to its phase difference approach, also apply to the low-pass behaviour of the linear deformation.

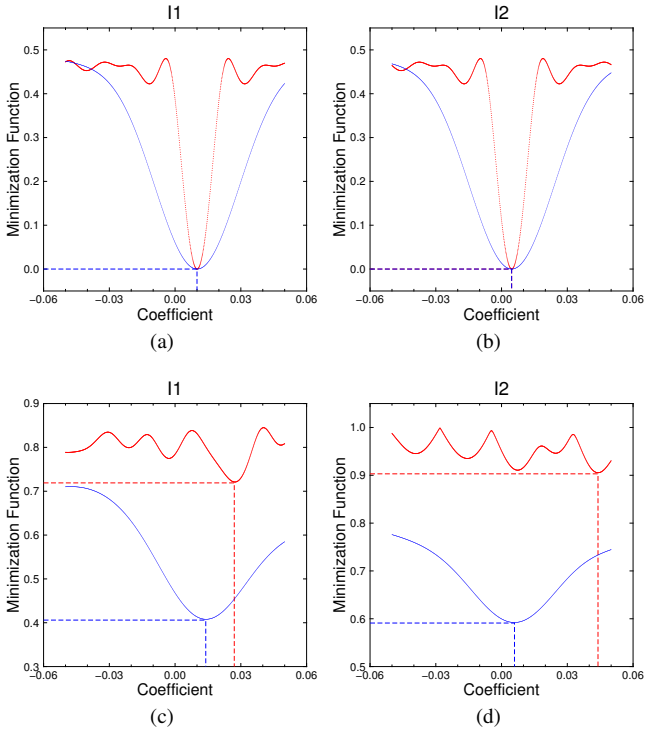

Fig. 4. Minimization Function. Red lines refer to conventional method and blue lines refer to D-LMRTA.

Besides explicit discussion on the above two interferograms I1 and I2, statistical analyses are carried out to evaluate the performance of LMRTA on other simulated pairs. Three methods are compared, conventional, unweighted LMRTA and covariance weighted V-LMRTA. Phase Standard Deviation (SD) is used as a metric to assess their performance. Detailed SD analyses are shown in Table III for four different pairs. Interferograms' phase components contain linear deformation, turbulent and stratified APS. *Reference phase* components include all of them except the stratified one. *Corrected phase*

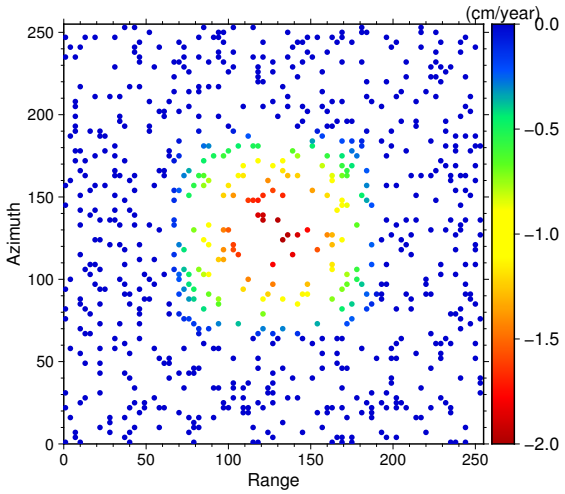

Fig. 5. Linear deformation pattern in simulated interferograms.

means residue after removing the estimated stratified component. The magnitude of the simulated turbulent APS is determined with the parameter $\sigma(0)$. The larger $\sigma(0)$ the stronger the turbulent component. As it can be seen in Table III, for a mild turbulent component (Ifg1, $\sigma(0) = 0.710$), all three methods provide a good estimation of stratified APS. More specifically, SDs of the corrected phases are close to the reference one, SD (0.514), and the relative errors are very small. Even though the differences are not significant, the smaller error is for V-LMRTA. When the turbulent component increases the performance of the conventional method starts to degrade. Ifg2, Ifg3 and Ifg4 show different cases with raising turbulent component. As expected, the relative errors for the conventional method raise as well. At the same time both LMRTA methods keep the relative errors small. The worst value for unweighted LMRTA is 2.732% and for V-LMRTA is 1.035%, but they do not occur with the interferogram with strongest turbulent APS. Once again, the best performance is provided by V-LMRTA.

Finally, a statistical comparison is applied to a set of 135 simulated interferograms with $\sigma(0)$ ranging from 0.71 to 3.53. The results are shown in Table IV. For the correction with conventional method only 39% pairs have a relative error below 1.5% while this rate increases dramatically to around 70% for both LMRTA. The number of pairs with relative error above 5.0% decreases from the 44.4% obtained with the conventional method to only 3.7% for both LMRTA. Meanwhile, the two LMRTA methods show a similar statistical performance. Moreover, a scatter plot for the 135 simulated interferograms relating $\sigma(0)$ and absolute SD error is shown in Fig. 6. It is clear that all the three methods present similar performances in interferograms with mild turbulent components. The better performance of LMRTA is evident in pairs with strong turbulent contamination.

IV. Test on Real Data

A. Test Site and Data Set

To demonstrate the performance of LMRTA on real data, Tenerife island (Spain, see Fig. 7) has been selected as test

TABLE III
PERFORMANCE OF DIFFERENT CORRECTION METHODS FOR FOUR SELECTED INTERFEROGRAMS. VALUES IN PARENTHESE ARE RELATIVE ERROR ($|Corrected - Reference|/Reference$).

Interferograms	$\sigma(0)$	Ifg phase SD	Reference phase SD	Corrected phase SD		
		All phase components	Components with no stratified APS	Conventional method	Unweighted LM-RTA	V-LMRTA
Ifg1	0.710	2.071	0.514	0.508 (1.167%)	0.509 (0.973%)	0.510 (0.778%)
Ifg2	1.574	1.834	1.546	1.761 (13.907%)	1.525 (1.358%)	1.530 (1.035%)
Ifg3	2.586	2.574	2.416	3.426 (41.805%)	2.482 (2.732%)	2.419 (0.124%)
Ifg4	3.310	3.235	2.547	3.491 (37.063%)	2.534 (0.510%)	2.535 (0.471%)

TABLE IV
STATISTICAL COMPARISON OF DIFFERENT CORRECTION METHODS FOR ALL SIMULATED INTERFEROGRAMS IN TERMS OF RELATIVE ERROR.

Correction performance	Numbers (Percentage)		
Relative error	Conventional method	Unweighted LMRTA	V-LMRTA
0-1.5%	53 (39.3%)	95 (70.4%)	94 (69.6%)
1.5%-3.5%	10 (7.4%)	24 (17.8%)	26 (19.3%)
3.5%-5.0%	12 (8.9%)	11 (8.1%)	10 (7.4%)
Above 5.0%	60 (44.4%)	5 (3.7%)	5 (3.7%)

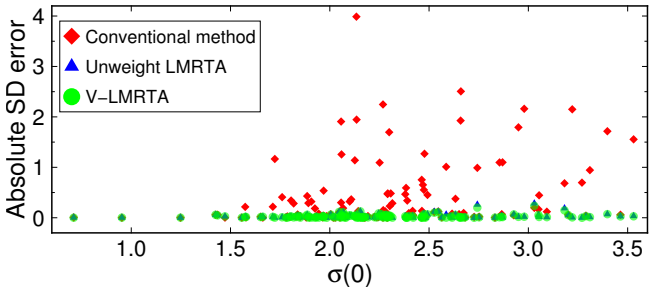

Fig. 6. The scatter plot between $\sigma(0)$ and absolute SD error for 135 interferograms with conventional, unweighted LMRTA and V-LMRTA methods.

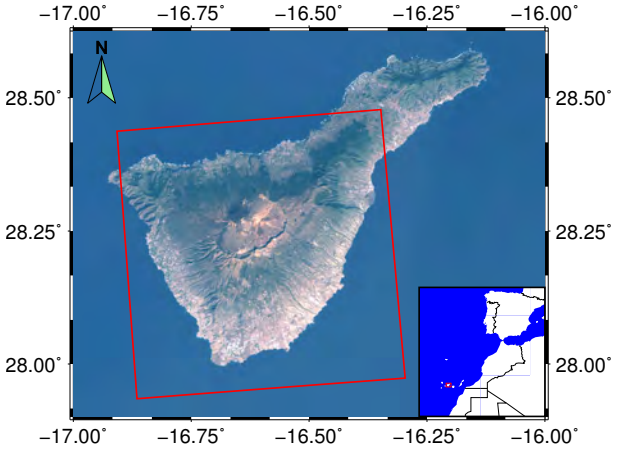

Fig. 7. Location of Canary Archipelago just off the southern coast of Morocco and map of Tenerife Island. The red rectangle indicates the area of interest, centred on Teide.

site. Tenerife is a volcanic island, whose eruptive system is dominated by the Las Canadas Caldera and the extinct volcano Teide. In 2004, a seismic crisis occurred in Tenerife, which produced surface gravity changes and displacements [38]. It is worth to point out that in this test site, the topography ranges from sea-level up to 3700 m. In such mountainous regions, the atmospheric artefacts can be deeply correlated with the topography. In addition, over coastal areas, atmospheric turbulences are usually strong [23], which can interfere the estimation of stratified APS with conventional methods. Consequently, this region is a perfect scenario to evaluate the correction capabilities of LMRTA. The dataset is composed by 55 Sentinel1-A satellite images acquired in the period covering from 2014 to 2016. From the available images 99 differential interferograms, with perpendicular and temporal baselines shorter than 400m and 70 days respectively, have been produced. All processing has been carried out with SUBSIDENCE-GUI, the software implementation of Coherent Pixel Technique (CPT) [5] developed at UPC.

By analysing the relationship between unwrapped phase and topography, it has been found that 14 out of the 99 interferograms present strong phase artefacts linearly correlated with topography. Fig. 8 shows 6 interferograms with different temporal and spatial baselines. The labels indicate the acquisition dates of the master and slave images with the format year-month-day (yyyymmdd). In order to exclude that the fringes were produced by inaccuracies of the DEM used to remove topography, Fig.9(a) shows a differential interferogram with a moderate baseline with almost no fringes on the slopes of Teide. Moreover, Fig. 9(b) shows a scatter plot of the spatial baseline and the number of fringes of the interferograms. Clearly, the number of fringes is not correlated with the spatial baseline. The performance of the proposed algorithm is assessed based on the aforementioned 14 pairs.

B. Processing Chain

The block diagram that summarizes LMRTA algorithm processing chain is shown in Fig. 10. As it can be observed, there are three main steps. Firstly, a preliminary linear model, which includes linear deformation and DEM error, is adjusted to the stack of multi-looked differential interferograms to cancel, as much as possible, the influence of these two phase components. Secondly, a weighted LMRTA model is adjusted to the residue phase to model stratified APS. Weighting can be obtained either from the covariance matrix or the pixels' distances. For the former, phase unwrapping is necessary

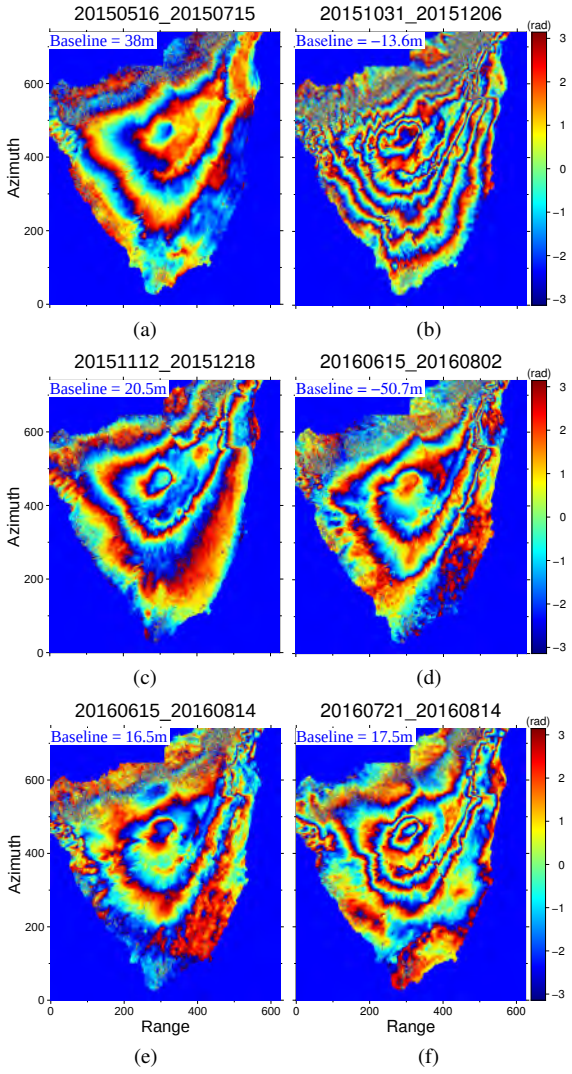

Fig. 8. Wrapped differential interferograms with strong topography-related APS.

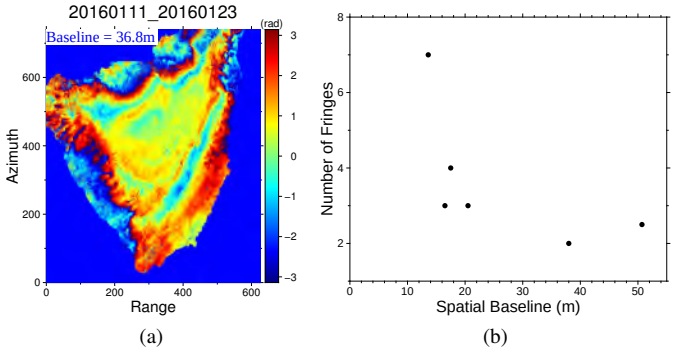

Fig. 9. (a) is the 20160111-20160123 differential interferogram. (b) is the relationship between the number of fringes and spatial baseline.

in order to estimate the covariance matrix from the experimental variogram. In this paper interferograms have been unwrapped using SNAPHU [39]. For the latter, unwrapping can be skipped. Once the topography correlated APS have been estimated with LMRTA, it can be removed from the interferograms. CPT is then applied to the compensated interferograms, which can be now at full-resolution, to determine the remaining velocity of deformation and DEM error. In practice, the first low-resolution linear model adjustment is affected by APS and the processing can be benefited by an iterative procedure, as shown in Fig. 10. The iteration over the residues does not need to recalculate the covariance matrix as the experimental variogram would not be reliable if residual phases were used. The iterative procedure helps to better estimate the stratified APS and the linear terms.

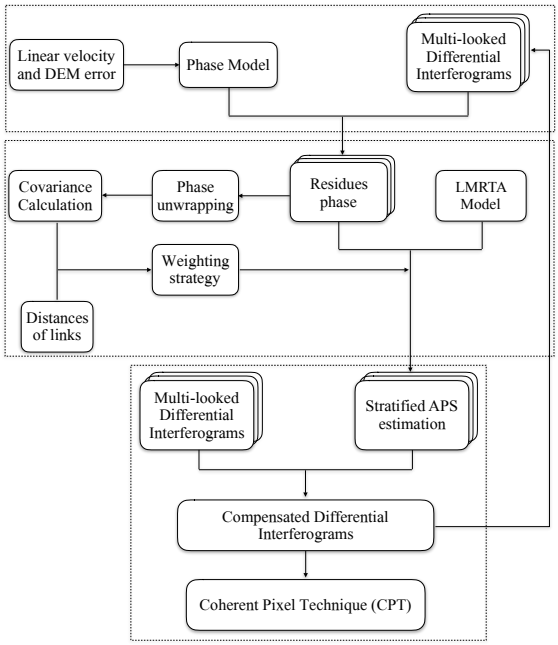

Fig. 10. LMRTA diagram for atmospheric artefacts compensation.

C. Stratified Atmospheric Artefacts Compensation

The performance of LMRTA is evaluated using Sentinel1-A data. Among all differential interferograms, the pair (20151031-20151206) has been selected to visualize the behavior of LMRTA. Firstly, pixels with coherence values higher than 0.7 from the multilooked, 5x25 (Azimuth x Range), interferograms are selected as PSs. The 15305 pixels selected are linked using a Delaunay triangulation to generate the observation vector $\Delta\phi_{obs}^{i,j}$. Then, equation (9) is applied to calculate the empirical variogram, and after that the covariance matrix using equation (11). Finally, conventional, unweighted LMRTA and V-LMRTA methods are used to retrieve the model coefficients that better fit the observation vector $\Delta\phi_{obs}^{i,j}$.

Fig. 11 presents the results using the different methods over the selected pair. In detail, Fig. 11(a) is the original wrapped differential interferogram, where fringes are strongly correlated with the topography. After the stratified APS compensation, wrapped residual phases for conventional linear model, unweighted LMRTA and V-LMRTA are shown in Fig. 11(b), Fig. 11(c) and Fig. 11(d) respectively. It is clear from the residual fringes that the three methods are able to reduce the number of fringes to some extent. To be specific, one evident fringe still exists in the residue after conventional correction, while there are no apparent topographic related fringes in the residues from both LMRTA, which produces visually almost

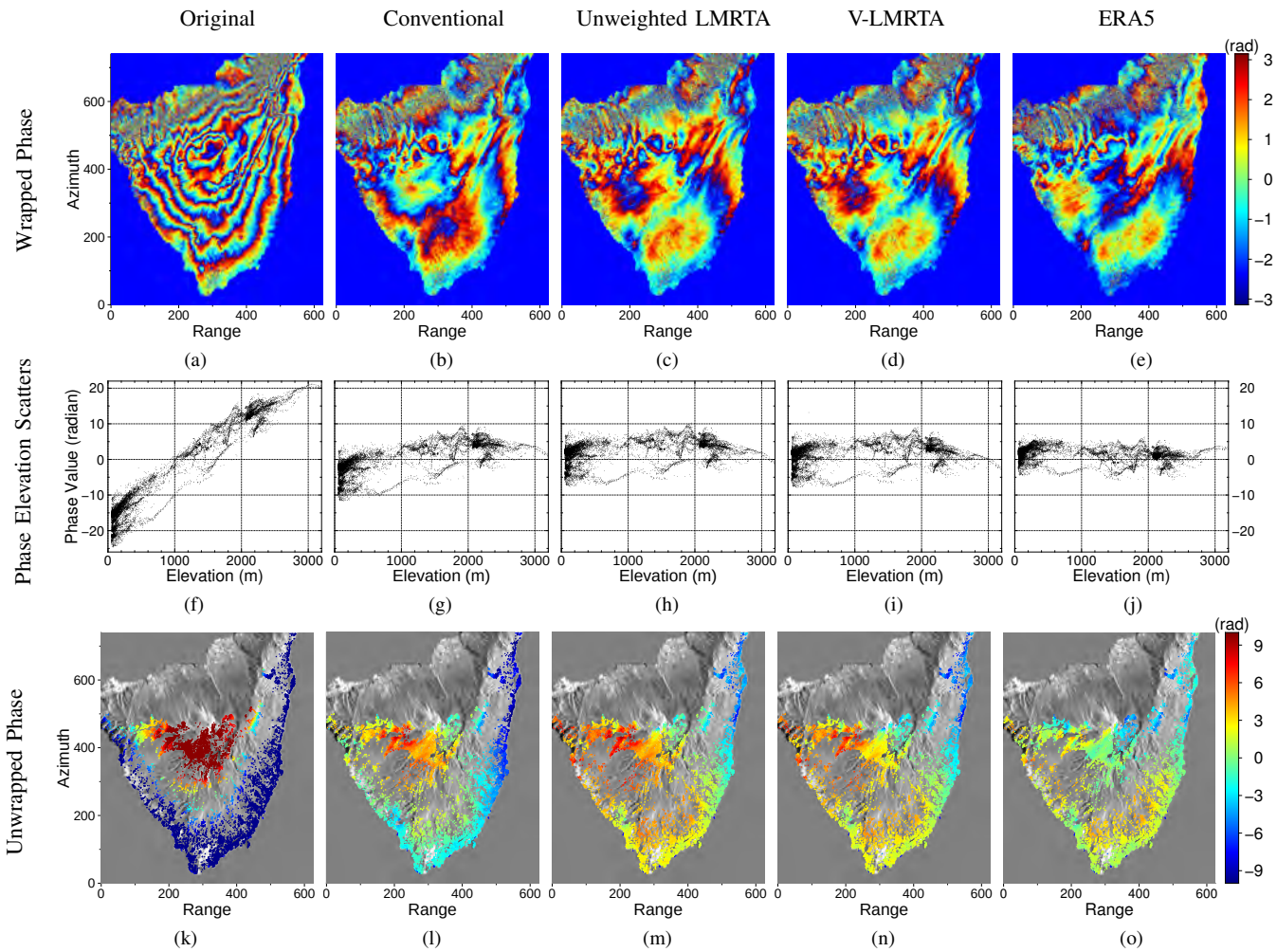

Fig. 11. One case study of APS compensation over Tenerife island, Spain. Columns from left to right show original phase, residue phase for conventional linear model, unweighted LMRTA, covariance weight V-LMRTA and ERA5 method respectively. Rows from top to bottom represent wapped phase, phase-elevation scatters and unwrapped phase residue.

identical results. The SD analysis on the unwrapped residue phases in subsection D shows that V-LMRTA performs better than unweightedt LMRTA. Unwrapped phases for differential interferograms and phase residues have been obtained with SNAPHU [39]. Subfigures in the second row of Fig. 11 show scatter plots of unwrapped phases and elevation of the selected PSs. It is clear from Fig. 11(f) that the unwrapped phase of the original differential interferogram shows a clear linear topographic trend. Conventional model and both LMRTA are able to correct this trend. An inspection of the phase residues shows the better performance of LMRTA compared with the conventional method, which still presents a residual linear trend as seen in Fig. 11(g). The third row in Fig. 11 shows the unwrapped phases of PSs over the radar brightness image. Once again, it is clear that LMRTA outperforms the conventional method.

The model adjustment could be benefited of an iterative procedure, as shown in Fig. 10, that would allow a refinement of the stratified APS estimation. The iterative procedure has been evaluated with the three methods using, as example, two different interferograms. The performance after each iteration is evaluated with the SD of the phase residue. Fig. 12(a) shows the 20151031-20151206 case, in which the three methods almost converge after the first regression. After the second iteration there is no significant improvement in the solution. As expected, V-LMRTA provides the solution with the lowest SD. Conversely, Fig. 12(b) shows a situation in which the conventional method diverges but unweighted LMRTA and V-LMRTA present identical performance as with the previous case. It can be concluded that the iterative procedure can refine the solution with just a single iteration and, in most of the cases, the marginal benefit obtained does not compensate its computational cost.

D. Validation with Global Meteorological Reanalysis Data

The proposed method is validated by comparing the phase delays estimated with those obtained from Global Atmospheric Models (GAMs) reanalysis data. ERA5 data has been selected for the validation as it is a relative new generation of climate reanalysis data with better performances than other datasets (e.g. ERA-interim, MERRA).

ERA5 is the fifth global European Center for Medium-Range Weather Forecasts (ECMWF) reanalysis product produced by Copernicus Climate Change Service, providing es-

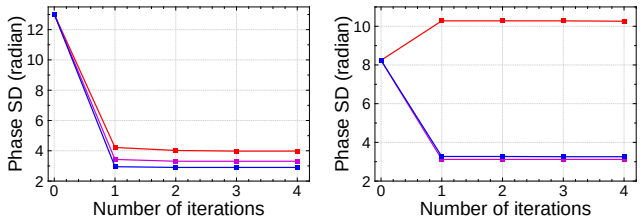

Fig. 12. SD of phase residues at each iteration. Red, magenta and blue represent conventional, unweighted LMRTA and V-LMRTA respectively. (a) 20151031-20151206 interferogram, (b) 20150715-20150808 interferogram.

timates of temperature, pressure, humidity and geopotential height along 37 pressure levels, with 31 km resolution. These reanalysis parameters are hourly available covering the period from 1979 to present [40].

Based on the vertical profiles of temperature, pressure, and relative humidity on coarse grid nodes provided by GAMs, the refractivity index N can be calculated with (2) at different height levels. Once the refractivity index N is computed, the absolute phase delay can be obtained for each pixel of the interferogram using (3). The integration of N along the LOS requires the interpolation of N at the required locations and an external DEM to consider the local topography of each pixel. Details on the derivation of tropospheric delays from the atmospheric reanalysis products are described in [16], [18], [41]. In this paper, based on the idea of integrating atmospheric parameters along zenith direction in Python-based Atmospheric Phase Screen (PyAPS) [16], [18], an improved method calculating APS along LOS direction [42] has been used to validate the algorithm.

Subfigures Fig. 11(e), Fig. 11(j) and Fig. 11(o) show the wrapped phase residue, the scatter plots of unwrapped phase residue versus elevation and the PSs unwrapped phase residue over the radar brightness image after ERA5 APS compensation. Comparing ERA5 result Fig. 11(j) with both LMRTA results Fig. 11(h) and Fig. 11(i), it can be observed that they look very similar. Both LMRTA and ERA5 phase residues present a similar magnitude and fluctuations around zero, despite the latter has a lower SD. This can be explained by the fact that ERA5 can remove the turbulent APS to some extent. However, phase residue from the conventional method (Fig. 11(g)) shows a linear trend, which is not consistent with ERA5 result.

After applying a statistical analysis on PSs unwrapped phases obtained from each method, it has been observed that unweighted LMRTA and V-LMRTA can reduce SD from 13.02 to 3.425 and 2.95 rad respectively, while SD from the conventional method is 4.22 rad. With ERA5 method, SD is reduced to 3.141 rad, which is closer to the results provided by V-LMRTA. The statistical comparison further validates that V-LMRTA outperforms the conventional linear method.

E. Statistical Analyses on All Interferograms

Besides detailed analyses on the above specific interferogram, a statistical comparison of original differential phases and phase residues using the different methods for 14 interferograms with significant stratified APS has been carried out. In the comparison, the phase SD is used as a quality metric and ERA5 APS is used as reference. As it can be seen from the original interferogram column in Table V, phase SD values are large due to the presence of strong atmospheric artefacts. After applying the different correction methods, SD of the phase residues are listed for each one.

Interferogram 20151112-20151218 (Ifg4) has been selected as example for a detailed analysis. Ifg4 was obtained from two images during the rainy season with a temporal baseline of 36 days and spatial baseline of 20.5 m. As it can be seen from Fig. 8(c), the wrapped phase exhibits a clear topography-related pattern that can be associated to stratified APS. After applying the conventional correction method, the SD of phase residue decreased a 51.0%, from 4.696 to 2.303 rad. Moreover, the residue can be reduced up to 1.649 and 1.678 rad using unweighted LMRTA and V-LMRTA respectively. Both LMRTA strategies produce similar results that are closer to the one provided by ERA5.

Another two interesting pairs (Ifg2 and Ifg13) show that SD phase residues even increased after applying the conventional method, while the other methods can reduce the phase residue to similar levels. For the particular case of Ifg13 the reduction is quite small. For all pairs in Table V except Ifg1, LMRTA based methods show more SD reduction than the conventional one. For Ifg1 case, the conventional method exhibits a correction of 51.5% compared with a 48.3% for the unweighted LMRTA and 46.7% for V-LMRTA, while ERA5 based correction shows the worst performance, 35.9%. The comparison between unweighted LMRTA and V-LMRTA shows that both produce comparable results in SD reduction and, depending on the case, one may achieve a better reduction than the other. The same idea can be applied to the ERA5 based compensation.

In all cases, both LMRTA strategies and ERA5 were able to reduce the APS but they are not able to cancel it completely. For the former, the turbulent APS is not considered in the linear model and thus it can not be compensated. For the latter, the coarse 30 km grid of the atmospheric parameters makes that strong local atmospheric artefacts would not be correctly modelled.

V. Conclusion

In this paper, a covariance weighted linear model for removing atmospheric artefacts in mountainous areas has been presented. The proposed approach, LMRTA, includes an improved linear model between stratified APS and topography based on phase differences among selected pixels, PSs, that reduces the impact of turbulent atmosphere. All selected pixels are related using a Delauney triangulation. The model adjustment step also considers a weighting strategy that minimizes the effect of those arcs between pixels affected by turbulent atmosphere. The weights can be obtained either from the spatial covariance matrix derived from the empirical variogram or simply penalizing the longer links that are prone to be affected by turbulent APS. The performance of this technique has been verified with simulated data and Sentinel1-A SAR data of Tenerife island.

TABLE V
PERFORMANCE OF DIFFERENT CORRECTION METHODS FOR 14 SELECTED INTERFEROGRAMS. VALUES IN PARENTHESES ARE CORRECTION PERCENTAGE, $(original - corrected)/original$.

Interferograms	Spatial baseline	Phase SD				
		Original interferogram	Conventional method	Unweighted LMRTA	V-LMRTA	ERA5
20150516-20150715 (Ifg1)	38.0 m	3.951	1.915 (51.5%)	2.044 (48.3%)	2.104 (46.7%)	2.533 (35.9%)
20150715-20150808 (Ifg2)	-30.7 m	8.239	10.283(-)	3.121 (62.1%)	3.169 (61.5%)	4.006 (51.4%)
20151031-20151206 (Ifg3)	-13.6 m	13.020	4.220 (67.6%)	3.425 (73.7%)	2.950 (77.3%)	3.141 (75.9%)
20151112-20151218 (Ifg4)	20.5 m	4.696	2.303 (51.0%)	1.649 (64.9%)	1.678 (64.3%)	1.818 (61.3%)
20151206-20151230 (Ifg5)	-8.6 m	2.063	1.850 (10.3%)	1.761 (14.6%)	1.773 (14.1%)	1.798 (12.8%)
20151218-20160216 (Ifg6)	-21.5 m	6.965	5.985 (14.1%)	5.365 (23.0%)	5.149 (26.1%)	4.414 (36.6%)
20160111-20160123 (Ifg7)	36.8 m	1.848	1.626 (12.0%)	1.592 (13.6%)	1.555 (15.9%)	1.526 (17.4%)
20160603-20160615 (Ifg8)	33.3 m	3.447	3.358 (2.6%)	2.541 (26.3%)	2.553 (25.9%)	2.603 (24.5%)
20160615-20160709 (Ifg9)	19.9 m	3.268	3.169 (3.0%)	2.464 (24.6%)	2.503 (23.4%)	2.533 (22.5%)
20160615-20160721 (Ifg10)	15.5 m	3.277	3.017 (7.9%)	2.569 (21.6%)	2.705 (17.5%)	2.770 (15.5%)
20160615-20160802 (Ifg11)	-50.7 m	5.644	3.575 (36.7%)	3.407 (39.6%)	3.183 (43.6%)	2.969 (47.4%)
20160615-20160814 (Ifg12)	16.5 m	4.581	2.871 (37.3%)	2.142 (53.2%)	2.203 (51.9%)	2.303 (49.7%)
20160709-20160826 (Ifg13)	30.8 m	3.014	3.448 (-)	2.863 (5.0%)	2.606 (13.5%)	2.477 (17.8%)
20160721-20160814 (Ifg14)	17.5 m	6.170	6.017 (2.5%)	2.407 (61.0%)	2.371 (61.6%)	2.925 (52.6%)

One important feature of the proposed algorithm is that topography related APS can be estimated from interferograms with no need of any auxiliary data, except a DEM. Besides, a distinctive advantage of the proposed approach is its robustness in situations where the interferogram contains turbulent APS or spatially low-pass deformation. The spatial covariance matrix, which characterises turbulent APS, is estimated from the interferogram itself. With the usage of covariance as a weighting strategy in the improved model, the influence of turbulent component can be reduced. As sometimes the estimation of the covariance matrix can be time consuming or prone to errors for heavily decorrelated interferograms, the weighting can also be established using the pixel's distance of each arc. Shorter arcs are considered to be more reliable in the model adjustment than longer ones.

Both simulated and real data have shown than LMRTA approach can robustly estimate the stratified atmosphere in presence of turbulent one and, partially, compensate APS in the interferograms. It is important to highlight the good agreement between LMRTA results and ERA5 based APS.

Further investigations will focus on more accurate variance-covariance matrix estimation, which is a critical step to characterise turbulent APS conditions.

ACKNOWLEDGMENT

The authors would like to thank Stanford Radar Interferometry Research Group for sharing SNAPHU package [39], and European Space Agency (ESA) for providing Sentinel1-A data. Figures in this paper were made with GMT software developed and maintained by Paul Wessel and Walter H. F. Smith.

REFERENCES

[1] R. F. Hanssen, *Radar interferometry: data interpretation and error analysis*. Dordrecht, The Netherlands: Kluwer, 2001.

[2] A. Ferretti, C. Prati, and F. Rocca, "Permanent scatterers in sar interferometry," *IEEE Trans. Geosci. Remote Sens.*, vol. 39, no. 1, pp. 8–20, 2001.

[3] P. Berardino, G. Fornaro, R. Lanari, and E. Sansosti, "A new algorithm for surface deformation monitoring based on small baseline differential sar interferograms," *IEEE Trans. Geosci. Remote Sens.*, vol. 40, no. 11, pp. 2375–2383, 2002.

[4] R. Lanari, O. Mora, M. Manunta, J. J. Mallorquí, P. Berardino, and E. Sansosti, "A small-baseline approach for investigating deformations on full-resolution differential sar interferograms," *IEEE Trans. Geosci. Remote Sens.*, vol. 42, no. 7, pp. 1377–1386, 2004.

[5] P. Blanco-Sanchez, J. J. Mallorquí, S. Duque, and D. Monells, "The coherent pixels technique (cpt): An advanced dinsar technique for nonlinear deformation monitoring," *Pure Appl. Geophys.*, vol. 165, no. 6, pp. 1167–1193, Jun. 2008.

[6] W. Gong, F. J. Meyer, S. Liu, and R. F. Hanssen, "Temporal filtering of insar data using statistical parameters from nwp models," *IEEE Trans. Geosci. Remote Sens.*, vol. 53, no. 7, pp. 4033–4044, 2015.

[7] P. Mateus, G. Nico, R. Tomé, J. Catalao, and P. M. Miranda, "Experimental study on the atmospheric delay based on gps, sar interferometry, and numerical weather model data," *IEEE Trans. Geosci. Remote Sens.*, vol. 51, no. 1, pp. 6–11, 2013.

[8] Z.-h. Li, "Correction of atmospheric water vapour effects on repeat-pass sar interferometry using gps, modis and meris data," Ph.D. dissertation, Univ. of London, London, United Kingdom, 2005.

[9] G. Wadge, P. Webley, I. James, R. Bingley, A. Dodson, S. Waugh, T. Veneboer, G. Puglisi, M. Mattia, D. Baker *et al.*, "Atmospheric models, gps and insar measurements of the tropospheric water vapour field over mount etna," *Geophys. Res. Lett.*, vol. 29, no. 19, pp. 11–1–11–4, Oct. 2002.

[10] F. Onn and H. Zebker, "Correction for interferometric synthetic aperture radar atmospheric phase artifacts using time series of zenith wet delay observations from a gps network," *J. Geophys. Res.–Solid Earth*, vol. 111, no. B9, Sep. 2006.

[11] J. S. Löfgren, F. Björndahl, A. W. Moore, F. H. Webb, E. J. Fielding, and E. F. Fishbein, "Tropospheric correction for insar using interpolated ecmwf data and gps zenith total delay from the southern california integrated gps network," in *Proc. IGARSS*, Honolulu, USA, 2010, pp. 4503–4506.

[12] D. Perissin, E. Pichelli, R. Ferretti, F. Rocca, and N. Pierdicca, "The mm5 numerical model to correct psinsar atmospheric phase screen," in *Proc. FRINGE*, Frascati, Italy, 2009.

[13] D. Perissin, F. Rocca, M. Pierdicca, E. Pichelli, D. Cimini, G. Venuti, and B. Rommen, "Mitigation of atmospheric delay in insar: The esa metawave project," in *Proc. IGARSS*, Vancouver, Canada, 2011, pp. 2558–2561.

[14] J. Foster, B. Brooks, T. Cherubini, C. Shacat, S. Businger, and C. Werner, "Mitigating atmospheric noise for insar using a high resolution weather model," *Geophys. Res. Lett.*, vol. 33, no. 16, Aug. 2006.

[15] G. Nico, R. Tome, J. Catalao, and P. M. Miranda, "On the use of the wrf model to mitigate tropospheric phase delay effects in sar interferograms," *IEEE Trans. Geosci. Remote Sens.*, vol. 49, no. 12, pp. 4970–4976, 2011.

[16] R. Jolivet, R. Grandin, C. Lasserre, M.-P. Doin, and G. Peltzer, "Systematic insar tropospheric phase delay corrections from global meteorological reanalysis data," *Geophys. Res. Lett.*, vol. 38, no. 17, Sep. 2011.

[17] J. Foster, J. Kealy, T. Cherubini, S. Businger, Z. Lu, and M. Murphy, "The utility of atmospheric analyses for the mitigation of artifacts in insar," *J. Geophys. Res.–Solid Earth*, vol. 118, no. 2, pp. 748–758, Feb. 2013.

[18] R. Jolivet, P. S. Agram, N. Y. Lin, M. Simons, M.-P. Doin, G. Peltzer, and Z. Li, "Improving insar geodesy using global atmospheric models," *J. Geophys. Res.–Solid Earth*, vol. 119, no. 3, pp. 2324–2341, Mar. 2014.
[19] J. Jung, D.-j. Kim, and S.-E. Park, "Correction of atmospheric phase screen in time series insar using wrf model for monitoring volcanic activities," *IEEE Trans. Geosci. Remote Sens.*, vol. 52, no. 5, pp. 2678–2689, 2014.
[20] F. Beauducel, P. Briole, and J.-L. Froger, "Volcano-wide fringes in ers synthetic aperture radar interferograms of etna (1992–1998): Deformation or tropospheric effect?" *J. Geophys. Res.–Solid Earth*, vol. 105, no. B7, pp. 16 391–16 402, Jul. 2000.
[21] O. Cavalié, M.-P. Doin, C. Lasserre, and P. Briole, "Ground motion measurement in the lake mead area, nevada, by differential synthetic aperture radar interferometry time series analysis: Probing the lithosphere rheological structure," *J. Geophys. Res.–Solid Earth*, vol. 112, no. B3, Mar. 2007.
[22] J. Elliott, J. Biggs, B. Parsons, and T. Wright, "Insar slip rate determination on the altyn tagh fault, northern tibet, in the presence of topographically correlated atmospheric delays," *Geophys. Res. Lett.*, vol. 35, no. 12, Jun. 2008.
[23] M.-P. Doin, C. Lasserre, G. Peltzer, O. Cavalié, and C. Doubre, "Corrections of stratified tropospheric delays in sar interferometry: Validation with global atmospheric models," *J. Appl. Geophys.*, vol. 69, no. 1, pp. 35–50, Sep. 2009.
[24] Y.-n. N. Lin, M. Simons, E. A. Hetland, P. Muse, and C. DiCaprio, "A multiscale approach to estimating topographically correlated propagation delays in radar interferograms," *Geochem. Geophys. Geosyst.*, vol. 11, no. 9, pp. 1–17, Sep. 2010.
[25] R. Iglesias, X. Fabregas, A. Aguasca, J. J. Mallorqui, C. López-Martínez, J. A. Gili, and J. Corominas, "Atmospheric phase screen compensation in ground-based sar with a multiple-regression model over mountainous regions," *IEEE Trans. Geosci. Remote Sens.*, vol. 52, no. 5, pp. 2436–2449, 2014.
[26] D. Bekaert, A. Hooper, and T. Wright, "A spatially variable power law tropospheric correction technique for insar data," *J. Geophys. Res.–Solid Earth*, vol. 120, no. 2, pp. 1345–1356, Feb. 2015.
[27] F. Chaabane, A. Avallone, F. Tupin, P. Briole, and H. Maître, "A multitemporal method for correction of tropospheric effects in differential sar interferometry: Application to the gulf of corinth earthquake," *IEEE Trans. Geosci. Remote Sens.*, vol. 45, no. 6, pp. 1605–1615, 2007.
[28] O. Mora, J. J. Mallorqui, and A. Broquetas, "Linear and nonlinear terrain deformation maps from a reduced set of interferometric sar images," *IEEE Trans. Geosci. Remote Sens.*, vol. 41, no. 10, pp. 2243–2253, 2003.
[29] J. Davis, T. Herring, I. Shapiro, A. Rogers, and G. Elgered, "Geodesy by radio interferometry: Effects of atmospheric modeling errors on estimates of baseline length," *Radio Sci.*, vol. 20, no. 6, pp. 1593–1607, 1985.
[30] A. L. Gray, K. E. Mattar, and G. Sofko, "Influence of ionospheric electron density fluctuations on satellite radar interferometry," *Geophys. Res. Lett.*, vol. 27, no. 10, pp. 1451–1454, May 2000.
[31] E. K. Smith and S. Weintraub, "The constants in the equation for atmospheric refractive index at radio frequencies," *Proc. Inst. Radio Eng.*, vol. 41, no. 8, pp. 1035–1037, 1953.
[32] S. H. Knospe and S. Jonsson, "Covariance estimation for dinsar surface deformation measurements in the presence of anisotropic atmospheric noise," *IEEE Trans. Geosci. Remote Sens.*, vol. 48, no. 4, pp. 2057–2065, 2010.
[33] N. Cressie, "Statistics for spatial data: Wiley series in probability and statistics," *Wiley-Interscience New York*, vol. 15, p. 16, 1993.
[34] G. Centolanza, "Quality evaluation of dinsar results from the phase statistical analysis," Ph.D. dissertation, Poly. Univ. Catalonia, Barcelona, Spain, 2015.
[35] C. Dietrich and G. Newsam, "A fast and exact method for multidimensional gaussian stochastic simulations," *Water Resour. Res.*, vol. 29, no. 8, pp. 2861–2869, 1993.
[36] B. M. Welsh, "Fourier-series-based atmospheric phase screen generator for simulating anisoplanatic geometries and temporal evolution," in *Symp. Opt. Sci., Eng. Inst.* International Society for Optics and Photonics, 1997, pp. 327–338.
[37] S. Liu, "Satellite radar interferometry: estimation of atmospheric delay," Ph.D. dissertation, Delft Univ. Technol., Delft, The Netherlands, 2012.
[38] J. Almendros, J. M. Ibáñez, E. Carmona, and D. Zandomeneghi, "Array analyses of volcanic earthquakes and tremor recorded at las cañadas caldera (tenerife island, spain) during the 2004 seismic activation of teide volcano," *J. Volcanol. Geothermal Res.*, vol. 160, no. 3, pp. 285–299, 2007.
[39] C. W. Chen and H. A. Zebker, "Two-dimensional phase unwrapping with use of statistical models for cost functions in nonlinear optimization," *J. Opt. Soc. Amer. A*, vol. 18, no. 2, pp. 338–351, 2001.
[40] H. Hersbach and D. Dee, "Era5 reanalysis is in production," *ECMWF Newsletter*, vol. 147, no. 7, 2016.
[41] N. Adam, "Algorithmic psi improvement in mountainous areas by atmosphere mitigation," *Terrafirma (ESA) Technical Note*, 2014.
[42] Z. Hu and J. J. Mallorquí, "A direct method to estimate atmospheric phase delay for insar with global atmospheric models," in *Proc. IGARSS*, Valencia, Spain, 2018, (in press).

Zhongbo Hu (S'16) was born in Hunan, China, in 1988. He received the bachelor's degree in geodesy and surveying engineering from the Central South University of Forestry and Technology, Changsha, China, in 2012. He is currently pursuing the Ph.D. degree with Universitat Politècnica de Catalunya (UPC), Barcelona, Spain.

He is currently with the Department of Signal Theory and Communications (TSC), UPC. His research interests include SAR data processing, differential SAR interferometry and atmospheric compensation algorithms for InSAR applications.

Jordi J. Mallorquí (S'93-M'96-SM'13) was born in Tarragona, Spain, in 1966. He received the Ingeniero degree in telecommunications engineering and the Doctor Ingeniero degree in telecommunications engineering for his research on microwave tomography for biomedical applications in the Department of Signal Theory and Communications from the Universitat Politècnica de Catalunya (UPC), Barcelona, Spain, in 1990 and 1995, respectively.

Since 1993, he has been teaching at the School of Telecommunications Engineering of Barcelona, UPC, first as an Assistant Professor, later in 1997 as an Associate Professor, and since 2011 as a Full Professor. His teaching activity involves microwaves, radionavigation systems, and remote sensing. He spent a sabbatical year with the Jet Propulsion Laboratory, Pasadena, CA, USA, in 1999, working on interferometric airborne synthetic aperture radar (SAR) calibration algorithms. He is currently working on the application of SAR interferometry to terrain deformation monitoring with orbital, airborne, and ground data; vessel detection and classification from SAR images; and 3-D electromagnetic (EM) simulation of SAR systems. He is also collaborating in the design and construction of a ground-based SAR interferometer for landslide control. Finally, he is currently developing the hardware and software of a bistatic opportunistic SAR for interferometric applications using European Remote Sensing, Environmental Satellite, and TerraSAR-X as sensors of opportunity. He has published more than 100 papers on microwave tomography, EM numerical simulation, SAR processing, interferometry, and differential interferometry in refereed journals and international symposia.

Hongdong Fan received the B.S. and M.S. degrees in Surveying and Mapping Engineering from the China University of Mining and Technology (CUMT), Xuzhou, China, in 2004 and 2007, respectively, and the Ph.D. degree in Geodetic and Surveying Engineering from CUMT, in 2010.

He is currently an associate professor with the school of Environment Science and Spatial Informatics, CUMT. His main research interests include DInSAR, advanced DInSAR, mining subsidence theory, and geological disaster monitoring.